

## ENGINEERING

# Wireless, fully implantable cardiac stimulation and recording with on-device computation for closed-loop pacing and defibrillation

Jokubas Ausra<sup>1†</sup>, Micah Madrid<sup>2†</sup>, Rose T. Yin<sup>2</sup>, Jessica Hanna<sup>1</sup>, Suzanne Arnott<sup>3</sup>, Jaclyn A. Brennan<sup>2</sup>, Roberto Peralta<sup>4</sup>, David Clausen<sup>1</sup>, Jakob A. Bakall<sup>1</sup>, Igor R. Efimov<sup>2,5,6\*</sup>, Philipp Gutruf<sup>1,7,8,9\*</sup>

Monitoring and control of cardiac function are critical for investigation of cardiovascular pathophysiology and developing life-saving therapies. However, chronic stimulation of the heart in freely moving small animal subjects, which offer a variety of genotypes and phenotypes, is currently difficult. Specifically, real-time control of cardiac function with high spatial and temporal resolution is currently not possible. Here, we introduce a wireless battery-free device with on-board computation for real-time cardiac control with multisite stimulation enabling optogenetic modulation of the entire rodent heart. Seamless integration of the biointerface with the heart is enabled by machine learning-guided design of ultrathin arrays. Long-term pacing, recording, and on-board computation are demonstrated in freely moving animals. This device class enables new heart failure models and offers a platform to test real-time therapeutic paradigms over chronic time scales by providing means to control cardiac function continuously over the lifetime of the subject.

## INTRODUCTION

Small animal models are useful tools for gaining key insights into development of pathologies and therapies, particularly in cardiovascular disease. Studies with rodents are particularly beneficial due to possibilities to engineer their genome to create more sophisticated models of cardiac failure. Rapid cardiac pacing can trigger pathogenesis of cardiovascular diseases, such as cardiomyopathy or atrial and ventricular fibrillation (1, 2). Electrical stimulation provides a method for probing these diseases but comes with the drawback of low cell specificity, damage to the stimulation site, and higher energy requirements (3–5). In contrast, optogenetic stimulation provides cell-specific stimulation to the cardiomyocytes or neurons of the heart (6). This selectivity allows for studies such as autonomic nervous control of the heart. Optogenetic stimulation in combination with electrical recording (7) provides a unique technique for studying arrhythmias where no cross-talk between the electrical sensing and optical stimulation can be leveraged (8). To achieve long-term in vivo studies where animals are untethered with freedom of movement, wireless pacemakers with on-board electrophysiological analysis and spatiotemporally accurate optical stimulation are required.

Implantable pacemakers, which are traditionally used for human therapies (9, 10), are useful for providing programmed electrical

stimulation during cardiac electrophysiology studies. However, with the development of highly miniaturized fully implantable pacemakers for rodents (11, 12), studies of cardiac electrophysiology can be expanded to transgenic small animal models (13–15). These developments can provide life-saving applications such as defibrillation of atrial fibrillation, defibrillation of ventricular fibrillation, and resynchronization therapy for patients with heart failure where cell-specific and multisite stimulation enabled by optogenetics are critical for successful implementation (16, 17). Multisite optical stimulation benefits studies exploring cardiac desynchrony with optogenetics, such as biventricular pacing (18), and combined with cell type-specific expression allows for an arrangement of neural and myocardial modulation studies, achievable with uniquely sensitive opsins (19). For example, in ventricular tachycardia (VT), multiple monophasic modulations are required to eliminate reentry for self-termination (20). While treating VT does not require multiple stimulation points, having the capacity to actuate from any required point on the heart is essential to stopping re-entry, because cardiac failure is a dynamic process with magnitude and locality of infarction changing from case to case clinically (21). In current technology, the computation of heart rate and the delivery of stimulation by these devices are achieved using multiple pieces of equipment or require researchers to interpret the data to determine and deliver the appropriate stimulus (22, 23). The spatiotemporal accuracy of these devices is often limited by the size of the interface that delivers stimulus to the heart, which, in turn, is limited by the lack of flexibility of the biointerface. As a result, the interface is restricted to a small section of the epicardium, which makes realization of multisite stimulation devices for specific animal models difficult (23).

In general, tethered devices are meant for short-term acute studies as they rely on fibers or cabled electrical connections to deliver stimulation and record heart rate and other data (18). While capabilities of tethered devices include closed-loop stimulation (24), the mechanical configuration is not suited for chronic implantation. The unification of chronic multisite cardiac interfaces, wireless

<sup>1</sup>Department of Biomedical Engineering, The University of Arizona, Tucson, AZ 85721, USA. <sup>2</sup>Department of Biomedical Engineering, The George Washington University, Washington, DC 20052, USA. <sup>3</sup>Department of Surgery, The George Washington University, Washington, DC 20037, USA. <sup>4</sup>Department of Aerospace and Mechanical Engineering, The University of Arizona, Tucson, AZ 85721, USA. <sup>5</sup>Department of Biomedical Engineering, Northwestern University, Chicago IL 60611, USA. <sup>6</sup>Department of Medicine (Cardiology), Northwestern University, Chicago, IL 60611, USA. <sup>7</sup>Department of Electrical and Computer Engineering, The University of Arizona, Tucson, AZ 85721, USA. <sup>8</sup>Bio5 Institute, The University of Arizona, Tucson, AZ 85721, USA. <sup>9</sup>Neuroscience Graduate Interdisciplinary Program (GIDP), The University of Arizona, Tucson, AZ 85721, USA.

\*Corresponding author. Email: pgutruf@email.arizona.edu (P.G.); igor.efimov@northwestern.edu (I.R.E.)

†These authors contributed equally to this work.

power transfer, and low-power real-time computational capabilities, as well as biopotential analog front ends, is required for these fully implantable embodiments, which are yet to be produced. Specifically, this includes adaptive geometries tailored for various heart shapes with high spatiotemporal accuracy and strategies for interface placement with mechanical, thermal, and chemical properties (13) that closely match the epicardium (12, 25).

Here, we present a wireless battery-free device with on-board computational capabilities, specifically high-fidelity heart rate detection, for closed-loop multisite optogenetics stimulation in small animal models. High spatiotemporal accuracy of stimulus delivery is achieved through the use of soft thin-film electrooptical arrays customized to deform with the beating pattern of the heart while providing continuous recording and optogenetic stimulation capabilities. The designs of the conformal arrays are tailored to fit the geometry of the animal heart. High-precision, personalized fabrication using laser structuring allows for rapid manufacturing and translation to a variety of animal models. In vivo experiments demonstrate the effectiveness of the customized device for pacing and recording with the potential for self-adjusting arrhythmia induction and defibrillation over chronic lifetimes.

## RESULTS

### Device overview

Critical for the deployment of fully implantable multifunctional and multisite cardiac interfaces for comprehensive manipulation of

heart function is the ability to record activity and intervene with real-time stimulation with ultralow latency to match the fast heart rate of small animal models. This is only possible with on-board computation, resulting in an intricate interplay among electromagnetics, digital and analog electronics, and mechanics to enable a platform that is fully implantable. A three-dimensional rendering of such a device implanted in a subject is shown in Fig. 1A. Here, a schematic depiction of a typical experimental paradigm of a freely moving animal subject inside an experimental arena delivering wireless power to the device to drive stimulation, recording, and computation components is shown. An animated exploded view rendering of constituent layers of the thin-film array conformally interfacing with the heart for high-fidelity electrical recording and optical stimulation is shown in the right-hand inset. Geometries are customized using deep learning software to provide the fit and mechanical compliance for continuous integration with the heart. The device body is located on the outside the animal's ribcage in the subcutaneous space to allow for wireless programming and communication of heart rate data with infrared (IR) uplink.

For these implantable devices, the size of the secondary antenna located on the device body must be considered to maximize the device's wireless harvesting capabilities to provide power to record, compute, and stimulate. To manage energy efficiently on the implant, temporary energy storage is used to buffer multisite simulation events in which the power required to operate the optoelectronic components (33 mW) exceeds the harvesting capabilities of the device (32 mW) in some operational scenarios. This can be accomplished

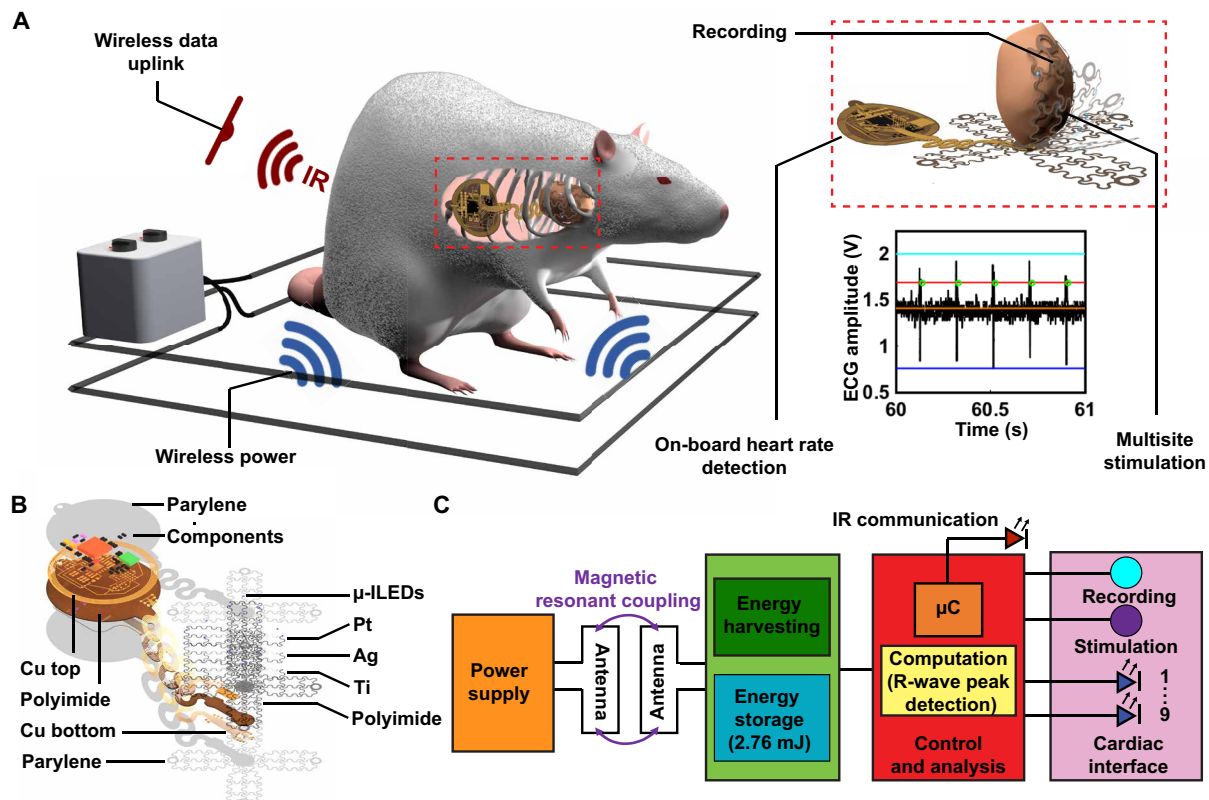


**Fig. 1. Device overview.** (A) Rendering of animal in typical experimental arena and inset highlighting device mechanics and operational capabilities. (B) Exploded view schematic showing layers of device. (C) Schematic diagram of operating electrical principles.

by taking advantage of highly miniaturized components to minimize device size as shown in the exploded view schematic in Fig. 1B, displaying the individual layers of the device. Here, the electronics for power harvesting, stimulation control, and on-board recording reside in the circular platform that connects to the thin-film array using stretchable serpentine interconnects to interface with the heart. The thin film of the array is composed of ultrathin layers of polyimide (PI), titanium, silver, and platinum to transfer energy to micro-scale inorganic light-emitting diodes ( $\mu$ -ILEDs) for illumination events and serve as electrodes for recording events while providing compliant mechanics for conformality. Detailed information on fabrication and material specifications can be found in Materials and Methods.

Magnetic resonant coupling (26) is used to harvest radio frequency (RF) power from the primary antenna (Fig. 1C). The harvested power is stored in a capacitor bank, and voltage is regulated by a linear, low dropout regulator and drives digital and analog electronics for computation, multisite stimulation, and electrical recording. Nine blue  $\mu$ -ILEDs are controlled by the microcontroller

( $\mu$ C). Amplification of the epicardial signals is performed by an ultraminiaturized analog front end on the device followed by analog-to-digital conversion and computational processing of heart rate on-board the  $\mu$ C. Detailed information on electronic components is presented in Materials and Methods.

### Mechanics

In comparison to our previous work on wireless optoelectronic devices for cardiac stimulation (12), the area of stimulation for this device is expanded by 1200% to allow for studies with high spatio-temporal accuracy. Because the size and shape of the heart vary from species to species, it is important to tailor the shape of the conformal array to fit the needs of a variety of phenotypes by designing the layout and mechanics based on analysis of geometry and beating patterns. Specifically, the ultrathin array interface to the heart is designed as shown in the flowchart diagram depicting this process in Fig. 2A. Here, a video of a representative perfused ex vivo mouse heart beating is recorded, a strategy that can also be applied to other animal models through similar methods or real-time

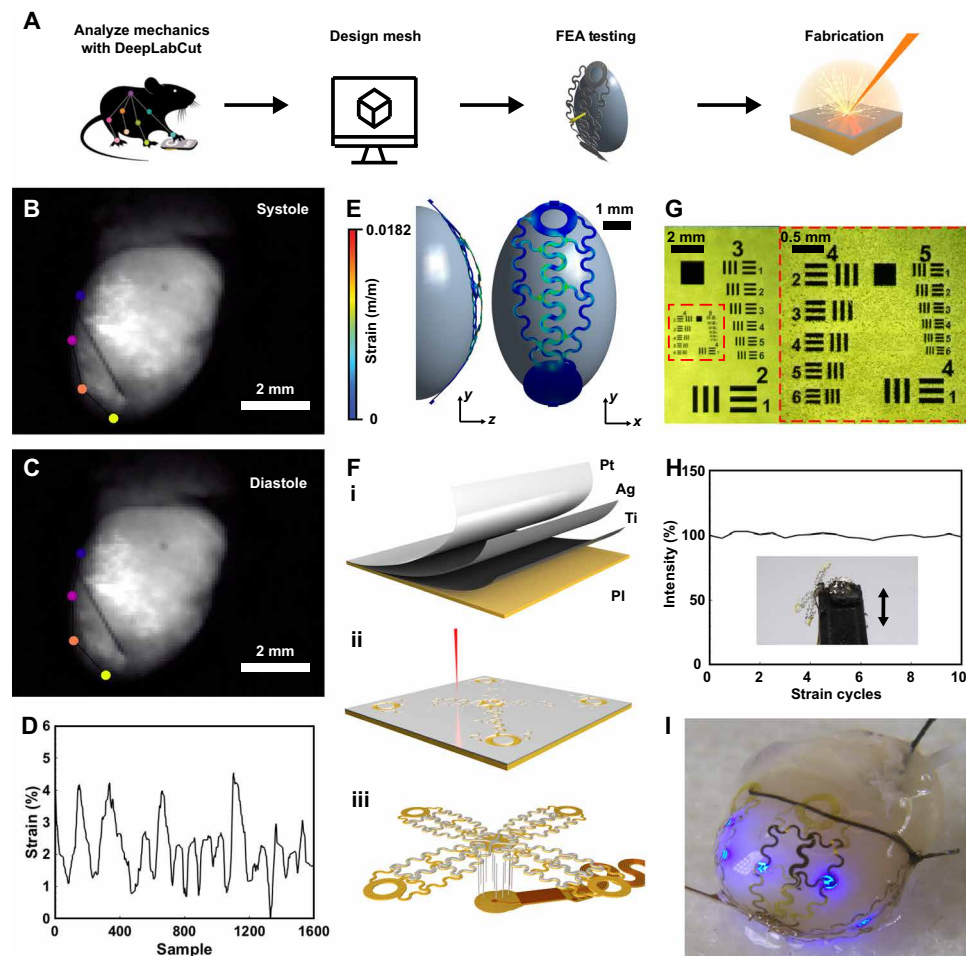


**Fig. 2. Mechanical design.** (A) Flowchart diagram of process for manufacturing  $\mu$ -ILED and recording array. FEA, finite element analysis. (B) Snapshot of heart with motion tracking markers during systole phase taken with optical mapping camera. (C) Snapshot of heart with motion-tracking markers during diastole phase. (D) Computed resulting strain during heart beating. (E) Mechanical simulation of heart deforming array. (F) Fabrication procedure of materials, (ii) laser structuring, and (iii) assembly of array onto device body. (G) Microscopic image of resolution test of laser structuring of metal thin films. (H) Ten thousand cycles of strain with irradiance output measurements of the  $\mu$ -ILED. (I) Photographic image of array applied to heart.

imaging modalities such as magnetic resonance imaging. The deep learning software DeepLabCut (27) analyzes the deformation of the heart using markerless tracking to compute change in surface area over beating cycles. The array is then designed using computer-aided design software, followed by simulation of the design via finite element analysis and iteration to enable elastic deformation of the constituent layers of the interface, and last, fabrication of the device using laser structuring, a process that can structure an array in 130 s without the need for clean room facilities.

To accurately determine the mechanical requirements for the array that allow the conductive structures to stretch without plastically deforming the thin metal film, deep learning software tracks the motion of the heart (Fig. 2, B and C) (see Materials and Methods for further detail). Here, distance between the four markers representing the changing circumference of the heart over several cycles of systole and diastole is calculated. The resulting elongation during cardiac cycles is found to be 4.5% of the original size, reflecting the required amount of cyclic strain durability of the device (Fig. 2D). In the material system used in the cardiac interface, the maximum allowable strain in the silver and platinum is 2.1 and 3.4%, respectively (28, 29), which cannot be exceeded without causing irreversible microcracking (30), reduction in trace conductivity (31, 32), and subsequent decrease in illumination and recording capabilities.

Achieving intimate contact between stimulation sites and the epicardium is challenging due to the expanse and contractility of the target organ. Using thin films organized in a repeating serpentine pattern (33), a flexible array is designed to fit the proportions of the heart and allow for elastic deformation as the heartbeats. The array consists of four petal-like structures containing one to three  $\mu$ -ILEDs each, with one petal housing the recording electrode. The structures adhere to the heart via a single suture that attaches to the ends of all petals. This geometry allows all sides of the heart to be enveloped, and application of the array is facile, allowing for rapid surgical procedures and fast animal recovery compared to bulkier telemetry systems for heart rate detection (34). With this unique design, which does not require epicardial sutures, we prevent tissue impact to the heart. Thin-film layers are carefully selected to enable maximum illumination while ensuring long-term recording capabilities over continuous strain cycles. Here, Ti deposited on PI thin film serves as an adhesion layer, followed by deposition of Ag for increased conductivity ( $6.30 \times 10^7$  S/m) (35). Pt is then deposited as the outermost layer due to its relatively high trace conductivity ( $9.43 \times 10^6$  S/m) (35) and the ability to serve as an oxidation-resistant chronic electrode to ensure long-term recording capabilities (36), thermal stability (37), and chemical stability (38).

The strain calculated from DeepLabCut tracking results is then applied in mechanical simulation in which the array undergoes an applied strain from an ellipsoid solid representing the heart perpendicular to the direction of the metal traces (fig. S1) (see Materials and Methods). This process is iterated to create a serpentine structure with mechanics to allow for elastic deformation of the metal layer to enable electrical conductance with chronic stability. In the finalized array design, the metal layer undergoes a strain of 1.82% when a global strain of 5% is applied, which is within the elastic regime of silver (2.1%) (28) and platinum (3.4%) (29) thin films (Fig. 2E).

Once the design of the stimulation and recording array has been finalized, fabrication begins with physical vapor deposition of titanium, silver, and platinum onto a thin film of PI (Fig. 2Fi). To

ensure rapid implementation of the device, fabrication with laser structuring avoids expensive and time-consuming clean room processes, thereby enabling unique array structures for a variety of animal models and even variation within species (Fig. 2Fii). Resolution of this method feature size of 20  $\mu$ m (Fig. 2G) provides sufficient flexibility in design and can accommodate even the smallest optoelectronic components. Attachment of the thin-film metal array onto flexible circuit materials is accomplished with through hole wiring (Fig. 2Fiii). Once components are added, fully constructed devices are encapsulated with parylene-C to provide a biofluid barrier (28). After encapsulation, laser ablation of the parylene-C from electrodes is completed as described in fig. S2. See Materials and Methods for further details.

The mechanical integrity of the array is verified with a custom stretching stage outfitted with a three-dimensionally (3D) printed heart that is used to flex the array at 1.4 Hz (fig. S3) (see Materials and Methods). A strain of 5% is applied to the array, representing the maximum deformation caused by the heart as calculated using deep learning software. To assess ability to remain conductive over beating cycles, illumination of the  $\mu$ -ILEDs of the array petal is quantified over 100,000 strain cycles and determined as stable (1.28% change in light intensity) (Fig. 2H), indicating that the structure can withstand several thousand strain cycles. Because of the high frequency of the rodent heartbeat, it is not possible to run accelerated cyclic tests; however, studies investigating thin-film metal strain durability indicate indefinite stability if no resistance change is observed after  $10^5$  cycles (39). Figure 2I shows a photographic image of an ex vivo mouse heart with the customized array applied, showing the ability to conform to the heart.

### Electrical characterization

The space available in small animal models requires a miniaturization of the device body. At the same time, recording, computation, and stimulation hardware as well as capacitive energy storage for high-intensity optogenetic stimulation events must be integrated onto a monolithic platform to ensure stable chronic operation. A detailed layout of the device with color coded elements is shown in Fig. 3A, and the corresponding electrical schematic is provided in Fig. 3B. The capacitor bank stores up to 2.76 mJ of energy when fully charged to 5.6 V. As energy is consumed for stimulation, the capacitor bank voltage drops to 3.5 V ( $\Delta 2.1$  V), the digital system operation voltage, resulting in 1.7 mJ of usable energy (40). The device relies on wireless power harvesting, which is maximized empirically by varying secondary antenna turns to enable maximum power output at the operation voltage of 3.5 to 5.6 V shown in Fig. 3C (see Materials and Methods). Here, the six-turn configuration outperforms the five- and seven-turn devices with a peak power of 32 mW in the center of the primary antenna at a load of 1.4 kilohms and a primary antenna power of 8 W. A 2D spatial map of the harvested power in a 22 cm-by-22 cm-by-6 cm arena is shown in Fig. 3D, where device power reaches over 100 mW in the corners of the arena. Because stimulation events require slightly more power (33 mW) compared to harvested power (32 mW), capacitive energy buffers stimulation events for continuous operation. This is achieved by storing energy in the capacitor bank between pulses (up to 1.7-mJ usable energy) and releasing stored energy during stimulation. This is enough energy to operate  $\mu$ -ILEDs at 101 mW/mm<sup>2</sup> for 1.5 s at a 100% duty cycle, which is far beyond the required on-time needed for high-powered stimulation events such as defibrillation (23).

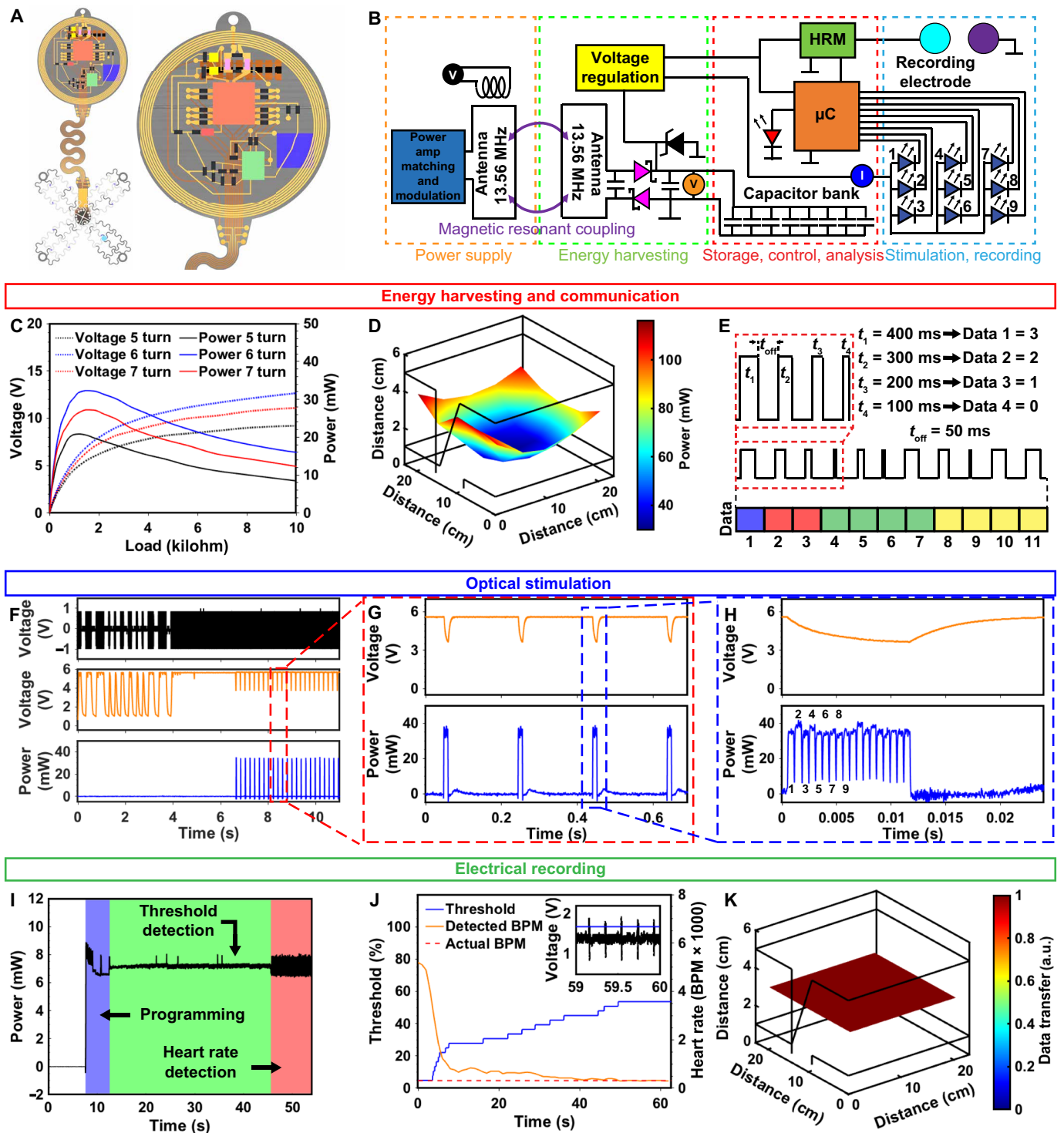


**Fig. 3. Electrical characterization.** (A) Rendered image of device highlighting component layout. (B) Electronic schematic of device with voltage and current probes indicated (C) Power versus load curve for device at center of 22 cm-by-22 cm arena powered at 8 W. (D) Spatial mapping of power distribution for device in 22 cm-by-22 cm-by-6 cm arena configured in a dual loop arrangement powered at 8 W. (E) Wireless communication scheme indicating bytes for program selection (blue), number of  $\mu$ -LEDs (red), frequency (green), and duty cycle (yellow). (F) Modulation principle showing pickup coil voltage (black), capacitor bank voltage (orange), and  $\mu$ -LED power (blue) with zoomed in view for (G) single second and (H) millisecond time scales. (I) Device power consumption during recording event. (J) Graph of device threshold voltage and resulting detected heart rate during automatic thresholding event. (K) Spatial distribution map of uplink stability. a.u., arbitrary units; BPM, beats per minute.

Wireless control of the device is accomplished using a custom simplex protocol as described previously (40, 41) to set parameters such as duty cycle, frequency, and the number of  $\mu$ -ILEDs activated. Figure 3E shows a diagram of the wireless communication scheme used for pacing and electrophysiological recording state selection. Here, 4-bit communication is accomplished by pulse width modulation via a commercial RF power source (NeuroLux Inc.) and custom modulation hardware. Pulses of 100 ( $t_1$ ), 200 ( $t_2$ ), 300 ( $t_3$ ), and 400 ms ( $t_4$ ) (representing logic bits 0, 1, 2, and 3) with 50 ms between pulses are used in this scheme. This configuration enables an increase of transmission speed of 500% and parameter space of 200% over our previous work (40). See Materials and Methods for more information on wireless communication.

Device power supply for a typical communication event is highlighted in Fig. 3 (F to H), with corresponding voltage and current probes displayed in Fig. 3B. Here, the magnetic field, which provides power to the implant, is modulated as indicated by the voltage of a pickup coil (black trace), which measures the strength of the magnetic field. Capacitor bank voltage (orange trace) follows the magnetic field strength, powering the  $\mu$ C for a specific amount of time during which internal timers digitally encode bit values that are written into the nonvolatile memory electrically erasable programmable read-only memory (EEPROM). Once all bit values have been defined, they are compiled into byte values for device operational parameters. Stimulation state is then selected after the  $\mu$ C evaluates the byte code; in this case, the device is set to turn all  $\mu$ -ILEDs on for multisite pacing. Specifically,  $\mu$ -ILEDs are multiplexed to turn on sequentially, so that stimulation site of the heart begins at the first  $\mu$ -ILED and is spatiotemporally cycled until reaching the ninth  $\mu$ -ILED to enable maximum illumination intensity at each site. Power of the  $\mu$ -ILEDs (blue trace) indicates that 32 mW are consumed for powering the  $\mu$ -ILEDs while operating at 5 Hz, with all nine  $\mu$ -ILEDs (labeled 1 to 9) cycling twice. All  $\mu$ -ILEDs were set to output an irradiance of 101 mW/mm<sup>2</sup>. See Materials and Methods for more details.

Figure 3I shows the power consumption of the device during recording where the blue background indicates a programming event in which the device uplinks a status report via the IR communication (42) (as selected via the programming in Fig. 3F), followed by the threshold detection of the cardiac pulse shown in the green background, and the heart rate computation and subsequent result uplink as indicated by the red background. Recording consumes an average of 7 mW of power throughout the programming, threshold detection, and heart rate detection events, with sufficient harvesting power to enable these operations indefinitely in freely moving animals.

Delivery of optogenetic stimulus can be managed with millisecond precision via on-board heart rate detection. This method bypasses the need for multiple electronic instruments to carry out recording and illumination by integrating both sensing and stimulation modalities into a monolithic platform with closed loop capabilities. To accurately detect heart rate on-board the device, the  $\mu$ C uses automatic thresholding to determine the minimum voltage the signal must surpass to count as a peak (Fig. 3J). The signal is first sampled to determine the average voltage (1.3 V on the inset of Fig. 3J). The threshold is set to this voltage (blue trace), and the number of signals greater than the threshold is recorded (yellow trace). The threshold increases until the time between these signals is consistent, such as when only peaks of the R wave of the electrogram (EGM) are detected, and the threshold locks in. This methodology offers

advantages in pacing immediately after detecting a heartbeat, allowing for millisecond precision (fig. S4) optogenetic stimulation for chronic arrhythmia induction or termination. Rapid heart rates, such as during arrhythmias, can be sensed on-board the device, and optogenetic stimulation can be carried out in response for operator-free defibrillation or tachypacing. Heart rate data can also be read out to manage stimulation parameters manually, with heart rate data able to be uplinked from all areas of the cage as shown in Fig. 3K. The IR receivers used in the experiments are fully integrated circuits in small packages with a lens system, an optical filter, automatic gain control, a bandpass filter to improve the signal-to-noise ratio, and demodulator circuits that pass the digital data signal to an external  $\mu$ C for demodulation (see Materials and Methods). At background ambient irradiances of more than 1 W/mm<sup>2</sup>, the lower detection threshold is 0.00015 W/mm<sup>2</sup>. Although transmission is most effective when in direct line of sight with the receiver, the system can function in a variety of situations, including those with opaque enclosures or 3D elements that rely on indirect IR reflections.

High IR transparency of rodent fur permits efficient operation even when the device body is fully implanted (42). Ex vivo experiments demonstrate transmission capability through tissue even when not in line of site, as shown in the fig. S5 and Materials and Methods.

### Optoelectronic characterization

Devices are designed for a variety of stimulation paradigms to, for example, invoke irregular heartbeats for cardiac pathology research. Figure 4A shows a photographic image of the stimulation and recording array with 9  $\mu$ -ILEDs powered on, capable of evoking strong activity in ChR2-expressing cardiomyocytes sufficient to defibrillate. The coverage of heart tissue with  $\mu$ -ILED illumination allows for targeting both ventricles, with multiple  $\mu$ -ILEDs simultaneously. Understanding thermal and optical characteristics of the heart tissue in response to activation of  $\mu$ -ILEDs is crucial for maintaining homeostasis and determining the extent of optogenetic influence on the deeper myocardial tissue of the heart. Measurements to quantify these parameters are carried out using an experimental setup for measuring temperature and light propagation in the heart as shown in the schematic of the lower half of Fig. 4A, where the device is applied to the interface of the heart. Photographic images of the setup are shown in fig. S6. Optical measurements are performed immediately adjacent to the  $\mu$ -ILED and at increasing depths toward the direction of the center of the heart for electrical powers of 22, 32, and 42 mW supplied to the  $\mu$ -ILED (Fig. 4B) (see Materials and Methods). An irradiance of 101 mW/mm<sup>2</sup> is observed at the interface of the  $\mu$ -ILED and the surface of the heart for an input electrical power of 32 mW. Irradiance remains above the threshold for optogenetic activation up to 3 mm into the heart tissue. Assuming the radius of stimulation to be 3 mm, the irradiance from each  $\mu$ -ILED can activate an area of 28 mm<sup>2</sup>, resulting in a total area coverage of 254 mm<sup>2</sup>. These results indicate that the device can activate any spatial region of a typical mouse heart with a total surface area of 110 mm<sup>2</sup> (43).

Accelerated rate testing of the device lifetimes is performed by characterizing the  $\mu$ -ILED irradiance for a device submerged in phosphate-buffered saline (PBS) at 60°C. Figure 4C shows a graph of light intensity over time, demonstrating latest measured operation at 60 days in heated solution without notable fluctuation in

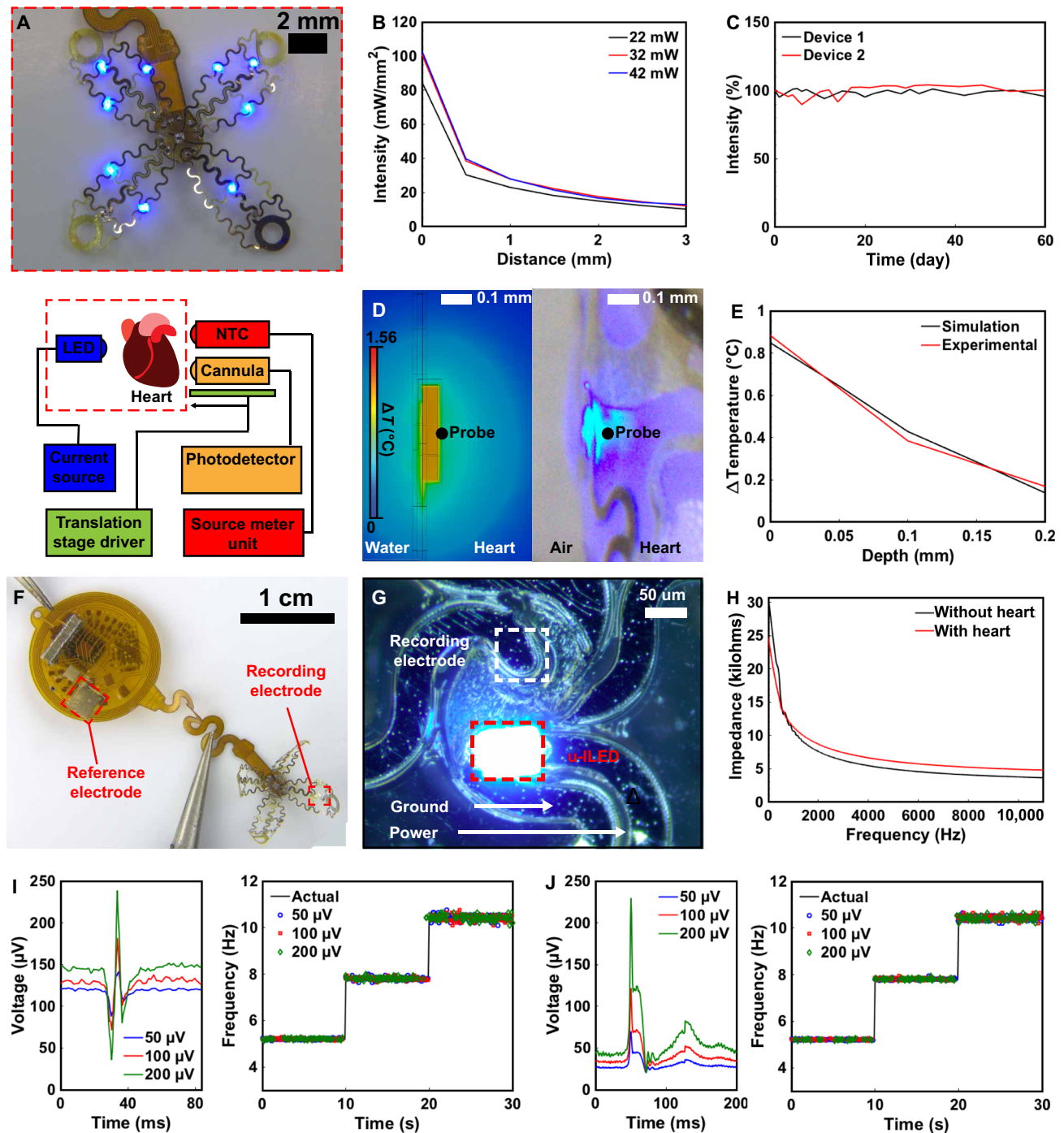


**Fig. 4. Optoelectronic characterization.** (A) Photographic image of  $\mu$ -LED and recording array (top) with schematic of setup used for optical and thermal measurement (bottom). (B) Device irradiance in cardiac tissue with increasing depths. (C) Graph of long-term irradiance measurements of device at 60°C in PBS. (D) Steady-state thermal simulation (left) and photographic image of experimental thermal measurements (right) for device operation at 40 Hz and 4% duty cycle. (E) Thermal load on cardiac tissue for device operated at 40 Hz and 4% duty cycle for simulation and experimental measurements. (F) Photographic image of device with reference and recording electrodes indicated. (G) Close-up photographic image of recording electrode and  $\mu$ -LED. (H) Graph of impedance at increasing frequencies for device in solution with and without heart present. (I) Input sinus rhythm waveform at three amplitudes (left) and resulting readout using on-board heart rate calculation for three frequencies (right). (J) Input waveform at three amplitudes (left) and resulting readout using on-board heart rate calculation for three frequencies (right).

irradiance. Fully implantable devices with similar accelerated test results had an estimated device lifetime of 205 days *in vivo* (44). See Materials and Methods for further details.

To avoid damage to cardiac tissue from high-power light pulses of the  $\mu$ -ILEDs, thermal load of the device on the heart is characterized. The thermal impact on the surface of the heart (left) during high-output optical events (right) is shown in Fig. 4D. Thermal finite element modeling is performed to assess changes in temperature in cardiac tissue at the site of the  $\mu$ -ILED for transient simulation and steady state to gain insight into thermal impact of the devices onto the cardiac tissue. The thermal impact on the surface of the heart (left) during high output optical events (right) is shown in Fig. 4D. During single  $\mu$ -ILED activation at 40 Hz with 1-ms on-time in finite element simulation (see Materials and Methods), a worst-case scenario (4% duty cycle) explored in other studies for optical defibrillation (23), the temperature change in the cardiac tissue during simulation (0.84°C) remained below the threshold for cardiac damage (45). In addition, thermal propagation characterization in mouse heart tissue *ex vivo* a temperature change of 0.89°C is observed, not considering perfusion (shown in fig. S7), verifying the finite element modeling simulations. Further chronic studies of thermal and photonic impact using this platform may inform device engineering for translational work toward chronic stability in the freely behaving subject. During *in vivo* experiments, it is also expected that thermal load on the heart further decreases due to perfusion (46) (see Materials and Methods for more information).

Figure 4F shows a photographic image of the device with recording and reference electrodes highlighted. The device uses a Pt recording electrode (2000  $\mu\text{m}^2$ ) that adheres to the epicardium and an Au reference electrode (6.75  $\text{mm}^2$ ) located on the device body. Figure 4G shows a photographic image of the device recording electrode and active  $\mu$ -ILED. This configuration allows for both pacing and stimulation in a compact area. Figure 4H shows a graph of impedance of the device electrodes in PBS solution with and without contact to cardiac tissue. A resulting impedance of 10.68 kilohms occurs at 1-kHz frequency in PBS and 11.35 kilohms on the heart tissue.

Real-time heart rate information is critical for stimulation paradigms such as optogenetic therapy for treating atrial fibrillation and realizing pacing-induced arrhythmias. Here, analog signals (Fig. 4I, left) are filtered and amplified by the analog front-end integrated circuit and sent to the  $\mu\text{C}$  for processing (see Materials and Methods for more information on recording characterization). After

automatic thresholding, timing between R waves is used to calculate the heart rate. Heart rate is detected for three tested frequencies of a typical cardiac waveforms within  $\pm 0.35$  Hz (Fig. 4I, right). The process is repeated for the waveform of an abnormal heartbeat (Fig. 4J, left), indicating that the on-board heart rate detection algorithm samples with  $\pm 0.24$ -Hz accuracy (Fig. 4J, right). In comparison, the typical accuracy for current commercially available wireless heart rate monitoring devices lies between  $\pm 0.2$  and  $\pm 0.6$  Hz (47). Thus, our device demonstrates on-board precision comparable to other devices used for wireless heart rate monitoring, which are critical for detecting abnormal heart rates, especially in the context of closed-loop operation where millisecond precision is vital for delivering stimuli.

### Ex vivo results

Functionality of optical pacing is verified in *ex vivo* Ch-R2 expressing mouse hearts using far-field electrocardiogram (ECG) recordings (Fig. 5A). Optoelectronic component layout of the device enables the study of cardiac resynchronization therapy or defibrillation (48).  $\mu$ -ILED modulation also enhances pacing parameters, permitting capturing at lower duty cycles and with lower irradiance. This reduction in duty cycle and irradiance brings clarity in optical mapping by lessening the interactions with potentiometric probes and the  $\mu$ -ILEDs, which diminishes optical artifacts in *ex vivo* studies (49). Figure 5B displays results where the heart is paced at 10 Hz (see Materials and Methods). Here, frequency of pacing capture is similar to previous studies on wireless battery free optogenetic pacing at 10 Hz (12) and allows for stimulation of a broader range of target sites.

In addition to optical pacing, electrical recording of *ex vivo* mouse hearts is assessed with far-field ECG. Results in Fig. 5C demonstrate the ability to capture heart rate on an *ex vivo* heart that has undergone external electrical stimulation with measured heart rate falling within  $\pm 0.14$  Hz of the set value (see Materials and Methods for more details). No notable deviation from regular heart rate is observed after the device is attached, arising from material selection and curvilinear design of the array that ensures conformality with the *ex vivo* heart without restricting motion. The simplicity of use and wireless battery-free operation suggests the utility of the device in a range of *ex vivo* Langendorff perfusion studies that monitor the heart during decline in cardiac performance from aging, mutation, pharmacological agents, or even environmental changes (50).

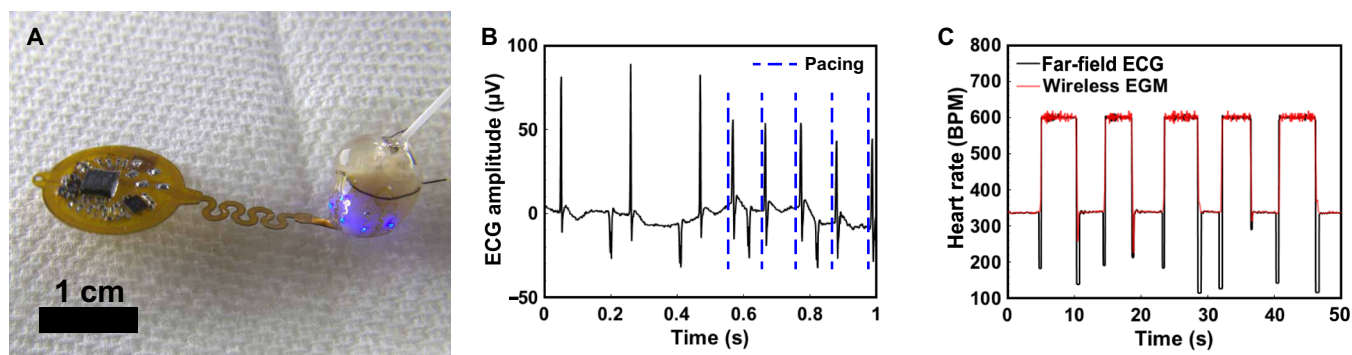


**Fig. 5. Ex vivo results.** (A) Photographic image of multisite pacing of *ex vivo* ChR2 expressing mouse heart. (B) ECG amplitude recorded from *ex vivo* ChR2-expressing mouse heart captured at 10 Hz, with blue lines representing the optical pacing stimulus. (C) Graph of wireless EGM versus far-field ECG recording during external electrical pacing on *ex vivo* heart.

## In vivo results

A flow diagram of the implantation procedure of the animal is shown in Fig. 6A. A customized implantation tool facilitates rapid surgery with facile placement and a quick securing mechanism to minimize the time the heart cavity is open. Here, a sterilized 3D-printed applicator attached to each petal of the device with water-soluble tape is used to position the device to envelop the heart (Fig. 6Ai and fig. S8). Once in place (Fig. 6Aii), the suture around the heart is tied and the tape is dissolved with saline, removing the connection between the applicator and the device (Fig. 6Aiii). The applicator is then removed (Fig. 6Aiv), and the device receiver is placed in the subcutaneous space, followed by closure of the muscle and skin by suture (see Materials and Methods for more information on implantation procedure). The animal recovers for 2 days upon receiving implantation of the optogenetic stimulation and recording device. Afterward, recording and pacing are performed on the animal to demonstrate wireless battery-free operation, computational ability, heart rate detection, and multisite optogenetic pacing capabilities. Figure 6B shows an image of the implanted device, highlighting the biointerface application to the left and right ventricles of the heart using a single suture that does not puncture the heart, allowing for seamless biointegration with the subject. This scheme minimizes scarring of the heart tissue while enabling multisite stimulation of the epicardium. Figure 6C shows a computed tomography (CT) image of the animal after device implantation, where the device position with respect to bone structure is indicated by the blue device body and serpentine interconnect leading to the array (see Materials and Methods). Animal recovery after implantation is assessed in Fig. 6D. The weight of the animal slightly decreases after surgery and appropriately increases over time, which illustrates that the device and its implantation result in no major postoperative complications, allowing for long-term recording and stimulation. The behavioral assessment of animals implanted with device cohabiting with a second control animal is also used to determine the effect of the implant on social interaction (Fig. 6E). Here, DeepLabCut tracking software is used to perform markerless tracking on animals before and after implantation as shown in the inset of Fig. 6E (see Materials and Methods). The results indicate that the animal has a similar number of social interactions 12 days postoperatively compared to before implantation (see fig. S9 for more information). On the basis of these results, this technology provides a route toward freely moving recording and stimulation for closed feedback applications in small animals while allowing for behavioral studies in naturalistic settings. This class of device offers advantages over tethered closed-loop devices for cardiac research by enabling the subjects to interact socially, thus increasing healing rate after implantation (51).

Stimulation and recording in a freely behaving subject are demonstrated Fig. 6F, where a labeled photographic image of the animal model shows the experimental setup that allows the animal to move in an unhindered fashion. Here, the animal sits inside the primary antenna that powers the device, with antenna frequency controlled by the tuning box and an IR receiver for recording wirelessly up-linked heart rate data. The heart rate of the freely moving animal subject is measured with the device and confirmed with far-field ECG as shown in the top graph of Fig. 6G. Demonstration of this capability can be found in movie S1. A bar graph of in vivo recorded heart rate in the animal several days after surgery is shown in the bottom of Fig. 6H, where an average heart rate of 500 beats per minute is observed on days 2, 3, and 12 in the wireless device with

on-board computation, which is expected for an adult mouse. These results show the potential for long-term studies that require heart rate measurements and stimulation. Adjacent results of chronic wireless battery-free neuromodulatory devices demonstrate operation over months and highlight the feasibility of this approach (52, 53). In addition to wirelessly measurement of heart rate, the device is able to pace the heart for chronic therapy or induction of heart rhythm disorders. Here, multisite pacing is captured on the far-field ECG in the top three graphs of Fig. 6H (see Materials and Methods for more details). Here, the number of  $\mu$ -ILEDs illuminating the epicardium is controlled wirelessly, allowing for tether-free studies in freely moving subjects. A comparison of the average R-wave amplitudes is shown in the bottom graph of Fig. 6H, where an increasing number of illumination sites results in higher R-wave amplitudes, as expected.

## DISCUSSION

The wireless battery-free platform for multimodal and multisite real-time stimulation, sensing, and computation presented here expands implantable cardiac device capabilities for on-demand operation in freely behaving small animal models. Devices are tailored for specific phenotypes individually using machine learning-guided mechanical design and cost-effective laser structuring to enable rapid device production for a spectrum of animal models. Specifically, serpentine structuring of ultralight thin films produces biointerfaces that closely conform to heart topology for mechanical integration with chronic device lifetimes. Surgical procedures are facilitated using custom-designed applicator tools to enable quick implantation.

The main obstacle for fully implantable devices with multisite stimulation, recording, and computation capabilities is tailoring the electromagnetic and mechanical characteristics to match the needs of the biological interface. Here, devices use on-board computational capabilities for heart rate monitoring to reduce size requirements associated with high-speed data transmission and allow for immediate feedback and action in real time on the monolithic platform. Advanced device communication allows for rapid selection of stimulation and recording states, and seamless integration of recording and stimulation modalities ensures millisecond precision feedback stimulation. These advances enable sensing, computation, and multisite stimulation to create complex experimental paradigms previously impossible for cardiac studies in freely behaving animals. Possible applications that build insight in small animal model studies include, defibrillation of atrial fibrillation affecting 5 million patients in the United States, defibrillation of ventricular fibrillation affecting 300,000 deaths in the United States annually, and resynchronization therapy for patients with heart failure affecting around 6 million patients in the United States (16, 17). These modalities showcased here offer new pathways for both cardiac pathological studies focused on the mechanisms of arrhythmogenesis and translational studies focused on development of antiarrhythmia therapy (i.e., defibrillation) in humans, which benefit substantially from cell-specific stimulation that can be a more efficient and pain-free alternative to current electrical methods. Remaining challenges include probing defibrillation mechanisms, modeling chronic heart rhythm disorders, and developing new multisite defibrillation and cardiac resynchronization therapy strategies. An opportunity afforded by wireless battery-free devices introduced here is the higher energy budget, which now enables computation on the edge with artificial intelligence to anticipate future cardiac events and gently intervene.

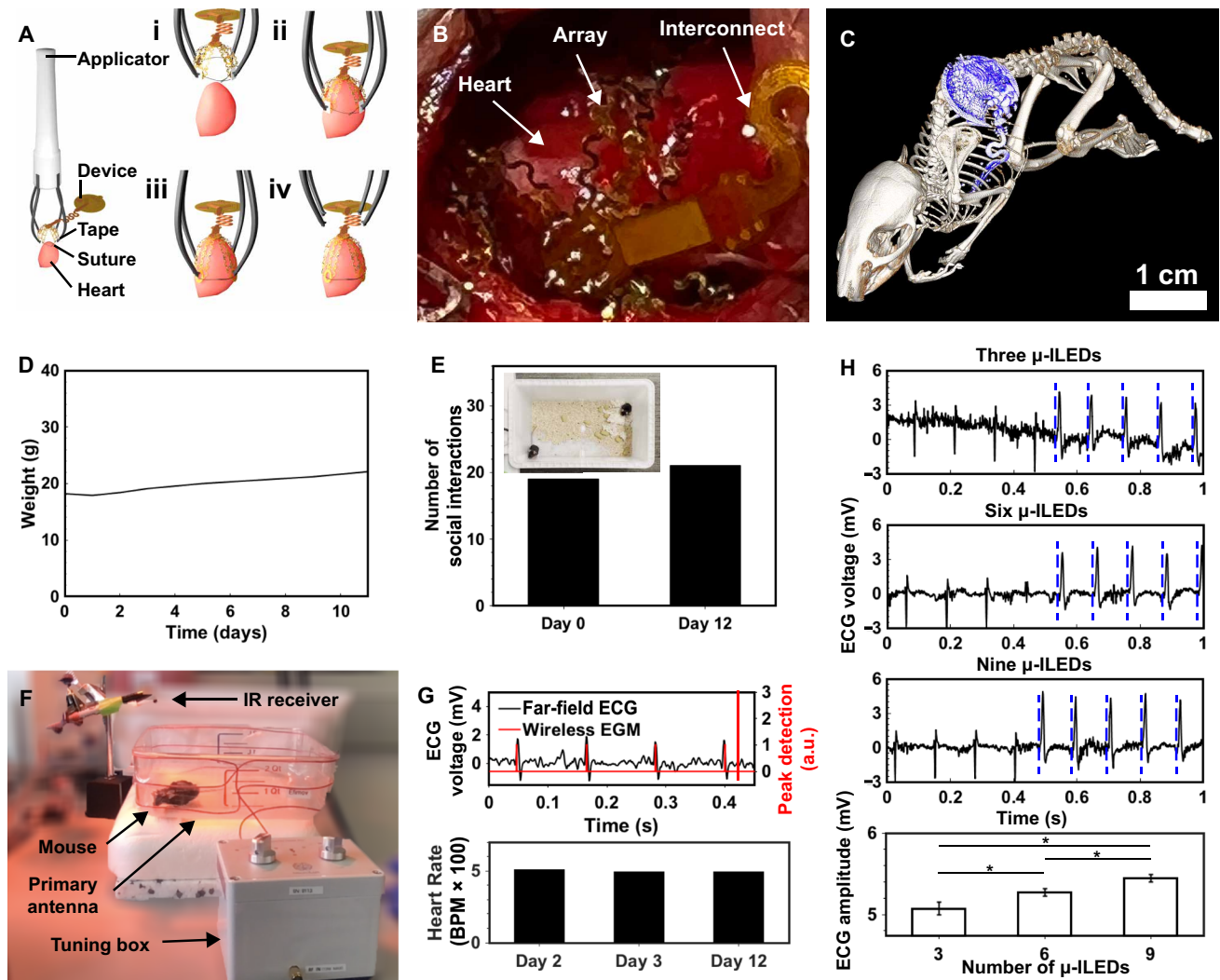


**Fig. 6. In vivo results.** (A) Implantation procedure showing (i) applicator with sutured mesh attached via dissolvable tape, (ii) application of mesh to heart followed by (iii) tape dissolution and suture tightening, and (iv) removal of applicator. (B) CT image of subdermally implanted device on the ribcage and heart of mouse. (C) In vivo surgical implantation of device on mouse heart. (D) Animal subject food intake and weight measurements postoperation. (E) Number of social interactions by animal subject before and after implantation over a 15-min period with inset showing arena used for behavioral tracking with neural network analysis. (F) Photographic image of freely moving animal subject during recording and stimulation. (G) Comparison of wireless EGM to far-field recording of freely moving animal subject (top) and wirelessly uplinked heart rates 2, 3, and 12 days after operation (bottom). (H) Graph of Chr2-expressing mouse heart in freely moving subject captured at 10 Hz using three, six, and nine  $\mu$ -ILEDs, with blue lines representing the optical pacing stimulus (top) and resulting amplitudes of QRS complexes presented as mean values  $\pm$  SE for three ( $n = 44$ ), nine ( $n = 44$ ), and nine  $\mu$ -ILEDs ( $n = 44$ ) (bottom).

## MATERIALS AND METHODS

### Device fabrication

Flexible circuits were constructed of Pylux AP8535R, and thin films were constructed using physical vapor deposition. High-precision laser structuring (LPKF U4) was used to structure the top and bottom copper layers (17.5  $\mu\text{m}$ ) on the PI layer (75  $\mu\text{m}$ ) substrate for the main body. The interface layers were composed of titanium (50 nm), silver (250 nm), platinum (50 nm), and a substrate layer of PI (18.5  $\mu\text{m}$ ). Flexible circuits were cleaned with flux (10 min; Superior Flux and Manufacturing Company, Superior no. 71) via ultrasonic cleaning (Vevor, Commercial Ultrasonic Cleaner), followed by isopropyl alcohol wash (2 min; MG Chemicals), and deionized (DI) water rinse. Via connections were constructed from copper wire

(100  $\mu\text{m}$ ) and low-temperature solder (Chip Quik, TS391LT). Device components were fixed in place after assembly with epoxy (TotalBoat), followed by curing at 80°C for 5 hours. Device electrodes were covered with water-soluble tape (polyvinyl alcohol) and PI tape. Devices were encapsulated with parylene-C coating via chemical vapor deposition. After encapsulation, laser structuring was used to remove parylene-C and PI tape, followed by dissolving of water-soluble tape in DI water for 24 hours at 40°C.

### Electronic components

Components with minimal outlines selected to minimize device footprint were manually soldered to the device using low-temperature solder (Chip Quik, TS391LT). The rectifier was composed of two

Shottky diodes (40 V, 30 mA; MCC RB751S-40DP), a tuning capacitor of 145 pF (CL03C101JB3NNNC), and a 2.2- $\mu$ F smoothing capacitor (Samsung, CL03A225MQ3CRNC). Eight 22- $\mu$ F capacitors (CL05A226MQ5QUNC) were assembled in parallel to serve as the capacitor bank (total capacitance of 176  $\mu$ F). A Zener diode (5.6 V, 100 mW; Comchip CZRZ5V6B-HF) provided overvoltage protection. Two low-dropout regulators with fixed internal outputs (3.5 V, NCP160AFCS350T2G; 2.8 V, TCR2DG28LF) managed voltage to the  $\mu$ -ILEDs and active components, respectively. A small outline  $\mu$ C (3 mm by 3 mm; ATtiny 84A, Atmel) was used to regulate timing of  $\mu$ -ILED activation, control on-board computing of heart rate, and IR uplink. The  $\mu$ C was programmed via AVR programmer and USB interface to sink current from the capacitor bank through the selected number of  $\mu$ -ILEDs at relevant time points. The irradiance of each  $\mu$ -ILED was controlled by the current limiting resistance of the thin film (18 ohms). A fully integrated single-lead small outline biopotential monitor (AD8233) was used to amplify and filter the readout of the electrodes. The  $\mu$ C firmware was programmed to digitize and automatically threshold the amplified signal. After thresholding, the time between detected pulses was uplinked via 0402 IR LED signal (57 kHz).

### RF characterization

The resonant frequency of the secondary antenna was verified to be 13.56 MHz by measuring the standing wave ratio with a reflection bridge (Siglent, SSA 3032X). Power harvesting capabilities of the secondary antenna for the five-, six-, and seven-turn devices were determined by placing each device on a 3-cm mount located in the center of the two-turn 22 cm-by-22 cm-by-6 cm cage powered at 8 W and measuring voltage output with increasing loads across the device using a digital multimeter (AN8008). The power distribution of the six-turn device throughout the arena was determined by measuring the secondary antenna output voltage with a load of 1.4 kilohms placed 3 cm from the cage floor throughout the arena with 4-cm spacing between each point.

### Electrical characterization

Electrical characterization during wireless state selection for stimulation and recording was carried out using a current probe (CurrentRanger, LowPowerLab) and oscilloscope (Siglent, SDS 1202X-E). Pickup coil voltage was determined by measuring unrectified voltage output of a six-turn secondary antenna tuned to resonate at 13.56 MHz to indicate the presence of magnetic field. System voltage was determined by measuring rectified voltage across the capacitor bank. Power consumption of the  $\mu$ -ILEDs was calculated by measuring current into the  $\mu$ -ILEDs at the defined system voltage. The device was powered using a custom battery power supply with current limiting resistor (560 ohms) in series to match the power input from the RF field for capacitor bank voltage measurements. Device power consumption during recording was determined by measuring the current into the  $\mu$ C and heart rate monitor at defined system voltage. Device threshold and heart rate data were uplinked via IR LED to an IR receiver using RC5 protocol (fig. S10).

### Wireless communication

Four-bit communication allowed for  $4^n$  states, where  $n$  represents the numbers in Fig. 3E. Sequences of pulses activated the information on the  $\mu$ C's nonvolatile memory (EEPROM). The first byte (blue; four states) relayed whether the device would record or stimulate.

The second byte (red; 16 states) determined the number of  $\mu$ -ILEDs for stimulation. The third and fourth bytes (green and yellow, respectively; 256 states each) sent frequency and duty cycle data, respectively.

### Recording characterization

Device on-board recording performance was determined by measuring the output heart rate of the device compared to the true input heart rate for input ECG waveform amplitude and frequency combinations of 50, 100, and 200  $\mu$ V and 5, 8, and 11 Hz. After automatic thresholding, output heart rates were calculated on-board the  $\mu$ C and uplinked to a receiver via IR communication.

### CT imaging

Micro-CT imaging was performed on a postmortem mouse using a Siemens Inveon  $\mu$ -CT scanner to take the images. Data were acquired with "medium-high" magnification, effective pixel size of 23.85,  $2 \times 2$  binning with 720 projections made in a full circle, and an exposure time of 300 ms. Peak tube voltage was set to 80 kV, and current of 300  $\mu$ A was selected to obtain the image of Fig. 5B. A Feldkamp cone-beam algorithm was used to reconstruct the data.

### Mechanical simulations

Mechanical simulations were performed in Ansys 2019 R2 Static Structural to assess the elastic strain in the serpentes when deformed by the heart. The conductive traces, PI substrate, and parylene-C encapsulation layers were combined into a single homogenous body to reduce computational complexity, and a single material with properties equal to the weighted composition of the cross section was used. The exact profile of the device was used. Program controlled mechanical elements were used to simulate the models with the resolution of the mesh elements being set to 2 and a sizing element condition of 0.03 mm on the heart mesh to ensure mesh convergence. The Young's modulus ( $E$ ) and Poisson's ratio ( $\nu$ ) for the combined material were  $EPI = 4$  GPa and  $\nu PI = 0.34$ , respectively. A fixed support was added to the top and bottom pieces of the mesh as shown in fig. S1. Displacements equivalent to those calculated with DeepLabCut of the heart were applied perpendicular to the mesh by deforming the heart over a total distance of 5% (0.3 mm).

### Strain testing

Mechanical strain of 5% (0.3 mm) was applied to the device by using a custom-built fatigue test setup with 3D-printed heart deforming the array (fig. S3). Arduino software was used to control the displacement.  $\mu$ -ILEDs were powered at 3.5 V using a custom battery supply and activated at 40 Hz with 1-ms on-time. Digital single-lens reflex camera (DSLR) camera was used to take images of the  $\mu$ -ILEDs every 5000 cycles in a custom-built darkbox. Manual focus was selected, iso was set to 100, F-stop was set to 36, and shutter speed was set to 1/250. The average light intensity from three  $\mu$ -ILEDs was calculated in ImageJ and plotted using MATLAB.

### Characterization of light propagation

The light propagation characterization in fresh mouse heart tissue was carried out using a custom translational stage and fiber optic cable (fig. S6). This system was composed of a 10-mm-long 0.22 numerical aperture optical fiber cannula (50- $\mu$ m core diameter) coupled to a high-sensitivity power meter (ThorLabs, PM100). A 3D-printed 1D linear translation stage was used to drive the cannula

into the heart. The blue  $\mu$ -ILED was attached to the heart via serpentine interconnect held up by suture. At each 1-mm step, three test powers were probed simultaneously (22, 32, and 42 mW). Light intensity was calculated by averaging over five values of illumination generated by the power meter. Preparations were set up within 1 hour before the characterization, including an intact heart. Data were acquired as the cannula was driven into the heart tissue to avoid unintentional scattering by air gaps created while retracting the fiber.

### Accelerated rate testing

Long-term characterization of device  $\mu$ -ILED irradiance as performed in a custom-built darkbox with DSLR camera for accelerated rate testing. Manual focus was selected, iso was set to 100, F-stop was set to 36, shutter speed was set to 1/4000 and 1/125 for devices A and B, respectively, and power of the NeuroLux was set to 8 W. Devices were placed in PBS solution (1%) at 60°C and measured every 1 to 5 days. The average light intensity from three  $\mu$ -ILEDs was calculated with ImageJ and plotted using MATLAB.

### Thermal simulations

Thermal finite element modeling was performed Ansys 2019 R2 to assess changes in temperature in cardiac tissue at the site of the  $\mu$ -ILED after 480 ms of stimulation for the transient simulation and steady-state thermal impact. Pacemaker body was simulated with accurate layouts and exact topologies for the PI, titanium, silver, platinum, and encapsulation layers. The resolution of the mesh was set to 6 with a minimum edge length of 0.325  $\mu$ m to ensure mesh convergence. The thermal conductivity and mass density of the materials used in the simulations were 130 W m<sup>-1</sup> K<sup>-1</sup>, 490 J kg<sup>-1</sup> K<sup>-1</sup>, and 8920 kg m<sup>-3</sup> for the  $\mu$ -ILED; 0.56 W m<sup>-1</sup> K<sup>-1</sup>, 3986 J kg<sup>-1</sup> K<sup>-1</sup>, and 1081 kg m<sup>-3</sup> for the epicardial tissue; 0.126 W m<sup>-1</sup> K<sup>-1</sup>, 837 J kg<sup>-1</sup> K<sup>-1</sup>, and 1110 kg m<sup>-3</sup> for the parylene encapsulation; and 0.12 W m<sup>-1</sup> K<sup>-1</sup>, 1090 J kg<sup>-1</sup> K<sup>-1</sup>, and 1420 kg m<sup>-3</sup> for the PI.

### Characterization of thermal propagation

Thermal propagation characterization in mouse heart tissue *ex vivo* was carried out using a custom-built temperature probe and positioning stage (fig. S6). A sourcemeter unit was used to measure millikelvin resolution values of tissue temperature from a 0201 negative-temperature coefficient sensor mounted to a custom probe (8.3 mm long, 0.5 mm wide, and 0.1 mm thick). The  $\mu$ -ILED was attached to the heart via serpentine interconnect held up by suture. After temperature sensor calibration, the 1D positioning stage was used to insert the temperature sensor probe opposite of the illumination site. Temperature measurements were taken at 0.1-mm increments starting from the location at the illumination site. For each measurement, the device was operated at 40 Hz and 4% duty cycle for 80 s. Afterward, the tissue was returned to ambient temperature via a cooldown period of 2 hours.

### Functional *ex vivo* testing

IR communication link was tested when an IR LED was subdermally positioned in a tissue sample including fur of a rodent subject (mouse, white fur). The IR LED was facing up toward the fur, and the digital communication IR receiver (Vishay Semiconductors; TSDP34156) was positioned with 8-cm source detector distance and increasingly angled (10° to 90°). The transmission rate was then calculated (fig. S5).

### Video tracking and motion analysis

Video tracking and motion analysis were used to assess changes in the deformation of cardiac tissue and to assess animal behavior before and after surgical implantation of the device. Videos for the cardiac deformation were recorded with an optical mapping camera (SciMedica Ultima L), and videos for the mouse behavior were recorded with a smartphone mounted above the animal in its home cage for 15 min. DeepLabCut Version 2.2.b6 was used for markerless tracking of the heart and head of the animals. Four locations of the heart were used for tracking cardiac displacement, and distinct body features (left ear and right ear) were used for the tracking animal movement. Training sessions of the heart and mouse model was accomplished with 37 s and 15 min of the recorded videos, respectively. The frame extraction rate of 78 frames/s was used to capture 37,000 and 27,000 frames from the videos of the heart and mouse, respectively. The training was computed with a high-performance computer (University of Arizona HPC) with 100,000 iterations for each assessment. Tracking was performed for 30 s for the video of the heart and 15 min for the videos of the mouse. Tracking data were exported as *x* and *y* coordinates along with confidence intervals and analyzed in excel. The data points with the confidence value greater than 92.5% were used for evaluating the total deformation of the heart and animal motion for the behavioral assessment.

### Mouse model

Animal procedures, as follows, were in accordance with the National Institutes of Health's ethical guidelines and performed with the approval of the Institute Animal Care and Use Committee of the George Washington University. The wild-type strain, C57BL/6 from the Jackson Laboratory, was used to assess recording capabilities and efficacy of implantation and defibrillation protocols. The commercially available ChR2(H134R)-EYFP mice, from the Jackson Laboratory, were used in all optogenetic experiments.

### Optogenetic pacing

Optogenetic pacing was performed on *ex vivo* mouse hearts. Optically expressing Ch-R2 mice were anesthetized using isoflurane until cessation of pain reflexes occurred, followed by the administration of heparin. With an open thoracotomy, the heart was quickly excised. After cannulation, hearts are placed in Langendorff tissue apparatus and perfused while being warmed and oxygenated (in 95/5% O<sub>2</sub>/CO<sub>2</sub>) in Tyrode's solution containing 128.2 mM NaCl, 4.7 mM KCl, 1.3 mM CaCl<sub>2</sub>, 1.05 mM MgCl<sub>2</sub>, 1.19 mM NaH<sub>2</sub>PO<sub>4</sub>-2H<sub>2</sub>O, 11.1 mM glucose, and 20 mM NaHCO<sub>3</sub>. Devices were attached via suturing of the loops of the four petals of the array to create close contact of the  $\mu$ -ILED's to the heart. Far-field ECG signals of the heart were recorded with LabChart (AD Instruments) by placing two recording and one reference electrode in the vicinity of the heart for the entirety of the experiment. An antenna circling the device tuned to 13.56 MHz (NeuroLux Inc) was then used to wirelessly power the device attached to the heart at 8 W to administer optical pacing to both ventricles of the heart with nine  $\mu$ -ILEDs activating at 10 Hz with a duty cycle of 1%. Optical stimuli capture was verified with ECG recordings.

### Electrical recordings

For on-board recording of the heart, a similar procedure as the one shown in the "Optogenetic pacing" section was followed. Wild-type

mice were specifically used to record the electrical activity of the heart. After the device recording electrode and heart were in contact, the device was wirelessly powered at 8 W and programmed to perform automatic thresholding, followed by IR uplink of on-board computed heart rate. Heart rates computed by the device were then verified with far-field ECG recordings.

### Surgical procedures

All surgical procedures used anesthetics and analgesics to start. The endotracheal tube was connected to the VentElite small animal ventilator (Harvard Apparatus) and kept the mouse anesthetized with 3% isoflurane and 97% oxygen. Buprenorphine (0.05 to 0.1 mg/kg) was introduced through subcutaneous injection with an addition of 0.25 ml of sterile saline. Toe pinches were performed to assess no signs of pain shortly after and every 5 min throughout experiment. The skin of the mice was incised with an Iris scissors two rib spaces above the left costal margin. Then, blunt dissection was carried down to the chest wall. Care was taken to enter the pleural space immediately superior to the rib and avoid injury to lung tissue when entering the thoracic cavity. At this point, elastic retractors were used to temporarily hold open incision and provide better visualization of the mediastinum. All incisions were closed with absorbable polyglycolic acid (4-0 to 5-0) for ribs and muscle and nonabsorbable nylon (4-0) for the skin. Analgesia was provided each day for 7 days post-operatively and then once each week after for up to 8 weeks to ensure minimizing pain. The animal was also closely monitored each dosage day to assess pain in home cages. The animal was weighed every 2 to 3 days for a total of 3 weeks.

### Chronic in vivo experiments

Optogenetic pacing and recording were performed beginning 1 day after implantation procedure. Devices were powered when the animal was placed in a cage with an antenna turned on at 8 W (NeuroLux Inc.). Pacing was performed at 7 and 10 Hz, with three, six, and nine  $\mu$ -ILEDs activated with 0.5-, 1-, 5-, and 10-ms on-times. Data from on-board heart rate detection were recorded using IR uplink to an IR receiver placed above the location of the animal. Freely moving animals underwent a similar procedure for both pacing and recording.

### Statistical analysis

For measuring statistical significance of ECG amplitude during optical stimulation, we performed a Student's *t* test with equal variance and a two-tailed distribution in Microsoft Excel. Significance was set at  $P < 0.05$ .

### SUPPLEMENTARY MATERIALS

Supplementary material for this article is available at <https://science.org/doi/10.1126/sciadv.abq7469>

### REFERENCES AND NOTES

- C. Riehle, J. Bauersachs, Small animal models of heart failure. *Cardiovasc. Res.* **115**, 1838–1849 (2019).
- M. Cerrone, S. F. Noujaim, E. G. Tolkacheva, A. Talkachou, R. O'Connell, O. Berenfeld, J. Anumonwo, S. V. Pandit, K. Vikstrom, C. Napolitano, S. G. Priori, J. Jalife, Arrhythmogenic mechanisms in a mouse model of catecholaminergic polymorphic ventricular tachycardia. *Circ. Res.* **101**, 1039–1048 (2007).
- C. M. Zgierski-Johnston, F. Schneider-Warme, Observing and manipulating cell-specific cardiac function with light. *Adv. Exp. Med. Biol.* **1293**, 377–388 (2021).
- J. C. Williams, E. Entcheva, Optogenetic versus electrical stimulation of human cardiomyocytes: Modeling insights. *Biophys. J.* **108**, 1934–1945 (2015).
- E. M. Wülfers, F. Schneider-Warme, A move in the light direction. *eLife* **10**, e65360 (2021).
- T. Bruegmann, D. Malan, M. Hesse, T. Beiert, C. J. Fuegemann, B. K. Fleischmann, P. Sasse, Optogenetic control of heart muscle in vitro and in vivo. *Nat. Methods* **7**, 897–900 (2010).
- F. Qian, C. Huang, Y.-D. Lin, A. N. Ivanovskaya, T. J. O'Hara, R. H. Booth, C. J. Creek, H. A. Enright, D. A. Soscia, A. M. Belle, R. Liao, F. C. Lightstone, K. S. Kulp, E. K. Wheeler, Simultaneous electrical recording of cardiac electrophysiology and contraction on chip. *Lab. Chip* **17**, 1732–1739 (2017).
- H. Cao, L. Gu, S. K. Mohanty, J.-C. Chiao, An integrated  $\mu$ LED optrode for optogenetic stimulation and electrical recording. *IEEE Trans. Biomed. Eng.* **60**, 225–229 (2013).
- B. W. Hale, D. J. Bradley, J. D. Zampi, W. Whiteside, R. Cunnane, First-in-human combined transcatheter tricuspid valve implantation with leadless VDD pacemaker via left internal jugular approach. *HeartRhythm Case Rep.* **8**, 155–159 (2022).
- I. Eltsov, A. Sorgente, C. de Asmundis, M. La Meir, First in human surgical implantation of a leadless pacemaker on the epicardial portion of the right atrial appendage in a patient with a cardiac electronic devices mediated dermatitis. *Interact. Cardiovasc. Thorac. Surg.* **35**, ivac050 (2022).
- J. I. Laughner, S. B. Marrus, E. R. Zellmer, C. J. Weinheimer, M. R. MacEwan, S. X. Cui, J. M. Nerbonne, I. R. Efimov, A fully implantable pacemaker for the mouse: From battery to wireless power. *PLOS ONE* **8**, e76291 (2013).
- P. Gutruf, R. T. Yin, K. B. Lee, J. Ausra, J. A. Brennan, Y. Qiao, Z. Xie, R. Peralta, O. Talarico, A. Murillo, S. W. Chen, J. P. Leshock, C. R. Haney, E. A. Waters, C. Zhang, H. Luan, Y. Huang, G. Trachiotis, I. R. Efimov, J. A. Rogers, Wireless, battery-free, fully implantable multimodal and multisite pacemakers for applications in small animal models. *Nat. Commun.* **10**, 5742 (2019).
- L. Xu, S. R. Gutbrod, A. P. Bonifas, Y. Su, M. S. Sulkin, N. Lu, H.-J. Chung, K.-I. Jiang, Z. Liu, M. Ying, C. Lu, R. C. Webb, J.-S. Kim, J. I. Laughner, H. Cheng, Y. Liu, A. Ameen, J.-W. Jeong, G.-T. Kim, Y. Huang, I. R. Efimov, J. A. Rogers, 3D multifunctional integumentary membranes for spatiotemporal cardiac measurements and stimulation across the entire epicardium. *Nat. Commun.* **5**, 3329 (2014).
- C. I. Berul, M. J. Aronovitz, P. J. Wang, M. E. Mendelsohn, In vivo cardiac electrophysiology studies in the mouse. *Circulation* **94**, 2641–2648 (1996).
- M. Ståhlberg, R. Nakagawa, D. Bedja, G. Zhu, B. L. Lin, A. Saberi, D. I. Lee, D. A. Kass, Chronic atrial and ventricular pacing in the mouse. *Circ. Heart Fail.* **12**, e005655 (2019).
- F. S. Ng, O. Toman, J. Petru, P. Peichl, R. A. Winkle, V. Y. Reddy, P. Neuzil, R. H. Mead, N. A. Qureshi, Z. I. Whinnett, D. W. Bourn, M. B. Shelton, J. Kautzner, A. D. Sharma, M. Hocini, M. Haïssaguerre, N. S. Peters, I. R. Efimov, Novel low-voltage multipulse therapy to terminate atrial fibrillation. *JACC Clin. Electrophysiol.* **7**, 988–999 (2021).
- J. Rickard, H. Michtalik, R. Sharma, Z. Berger, E. Iyoha, A. R. Green, N. Haq, K. A. Robinson, Use of cardiac resynchronization therapy in the Medicare population [internet] (National Center for Biotechnology Information, 2015); <https://pubmed.ncbi.nlm.nih.gov/26247085/>.
- U. Nussinovitch, L. Gepstein, Optogenetics for in vivo cardiac pacing and resynchronization therapies. *Nat. Biotechnol.* **33**, 750–754 (2015).
- L. Li, L. Lu, Y. Ren, G. Tang, Y. Zhao, X. Cai, Z. Shi, H. Ding, C. Liu, D. Cheng, Y. Xie, H. Wang, X. Fu, L. Yin, M. Luo, X. Sheng, Colocalized, bidirectional optogenetic modulations in freely behaving mice with a wireless dual-color optoelectronic probe. *Nat. Commun.* **13**, 839 (2022).
- W. Li, C. M. Ripplinger, Q. Lou, I. R. Efimov, Multiple monophasic shocks improve electrotherapy of ventricular tachycardia in a rabbit model of chronic infarction. *Heart Rhythm* **6**, 1020–1027 (2009).
- P. G. Masci, J. Ganame, M. Francone, W. Desmet, V. Lorenzoni, I. Iacucci, A. Barison, I. Carbone, M. Lombardi, L. Agati, S. Janssens, J. Bogaert, Relationship between location and size of myocardial infarction and their reciprocal influences on post-infarction left ventricular remodelling. *Eur. Heart J.* **32**, 1640–1648 (2011).
- E. C. A. Nyns, T. Jin, M. S. Fontes, T. van den Heuvel, V. Portero, C. Ramsey, C. I. Bart, K. Zeppenfeld, M. J. Schalij, T. J. van Brakel, A. A. Ramkisoensing, G. Zhang, R. H. Poelma, B. Ördög, A. A. F. de Vries, D. A. Pijnappels, Optical ventricular cardioversion by local optogenetic targeting and LED implantation in a cardiomyopathic rat model. *Cardiovasc. Res.* **118**, 2293–2303 (2021).
- L. Diaz-Maue, J. Steinebach, M. Schwaerzle, S. Luther, P. Ruther, C. Richter, Advanced cardiac rhythm management by applying optogenetic multi-site photostimulation in murine hearts. *JoVE*, e62335 (2021).
- H. Wen, J. Chunpeng, Q. Mu, S. Ziliang, J. Pengfei, W. Longchun, T. Kejun, L. Lijun, G. Zhejun, Y. Bin, W. Xiaolin, L. Jingquan, Self-adaptive cardiac optogenetics device based on negative stretching-resistive strain sensor. *Sci. Adv.* **7**, eabj4273 (2022).
- Y. S. Choi, R. T. Yin, A. Pfenniger, J. Koo, R. Avila, K. B. Lee, S. W. Chen, G. Lee, G. Li, Y. Qiao, A. Murillo-Berlitz, A. Kiss, S. Han, S. M. Lee, C. Li, Z. Xie, Y.-Y. Chen, A. Burrell, B. Geist, H. Jeong, J. Kim, H.-J. Yoon, A. Banks, S.-K. Kang, Z. J. Zhang, C. R. Haney, A. V. Sahakian, D. Johnson, T. Efimova, Y. Huang, G. D. Trachiotis, B. P. Knight, R. K. Arora, I. R. Efimov, J. A. Rogers, Fully implantable and bioresorbable cardiac pacemakers without leads or batteries. *Nat. Biotechnol.* **39**, 1228–1238 (2021).
- P. Gutruf, V. Krishnamurthi, A. Vázquez-Guardado, Z. Xie, A. Banks, C.-J. Su, Y. Xu, C. R. Haney, E. A. Waters, I. Kandel, S. R. Krishnan, T. Ray, J. P. Leshock, Y. Huang,

- D. Chanda, J. A. Rogers, Fully implantable optoelectronic systems for battery-free, multimodal operation in neuroscience research. *Nat. Electron.* **1**, 652–660 (2018).
27. A. Mathis, P. Mamidanna, K. M. Cury, T. Abe, V. N. Murthy, M. W. Mathis, M. Bethge, DeepLabCut: Markerless pose estimation of user-defined body parts with deep learning. *Nat. Neurosci.* **21**, 1281–1289 (2018).
  28. D. Kim, S.-H. Kim, J. H. Kim, J.-C. Lee, J.-P. Ahn, S. W. Kim, Failure criterion of silver nanowire electrodes on a polymer substrate for highly flexible devices. *Sci. Rep.* **7**, 45903 (2017).
  29. R. A. Meiroim, T. E. Clark, C. L. Muhlstein, The role of specimen thickness in the fracture toughness and fatigue crack growth resistance of nanocrystalline platinum films. *Acta Mater.* **60**, 1408–1417 (2012).
  30. P. Gutruf, S. Walia, M. Nur Ali, S. Sriram, M. Bhaskaran, Strain response of stretchable micro-electrodes: Controlling sensitivity with serpentine designs and encapsulation. *Appl. Phys. Lett.* **104**, 021908 (2014).
  31. Y. Wang, J. Cheng, Y. Xing, M. Shahid, H. Nishijima, W. Pan, Stretchable platinum network-based transparent electrodes for highly sensitive wearable electronics. *Small* **13**, 1604291 (2017).
  32. N. Lu, X. Wang, Z. Suo, J. Vlassak, Metal films on polymer substrates stretched beyond 50%. *Appl. Phys. Lett.* **91**, 221909 (2007).
  33. T. Widlund, S. Yang, Y.-Y. Hsu, N. Lu, Stretchability and compliance of freestanding serpentine-shaped ribbons. *Int. J. Solids Struct.* **51**, 4026–4037 (2014).
  34. D. Ho, X. Zhao, S. Gao, C. Hong, D. E. Vatner, S. F. Vatner, Heart rate and electrocardiography monitoring in mice. *Curr. Protoc. Mouse Biol.* **1**, 123–139 (2011).
  35. R. Serway, *Principles of Physics* (Saunders College Pub., ed. 2, 1998).
  36. H. Wadullah, S. Ajeel, M. Abbass, Corrosion of platinum nanocoatings thin films deposited by sputtering deposition method for medical applications. *Int. J. Eng. Technol.* **7**, 63–66 (2018).
  37. S. L. Firebaugh, K. F. Jensen, M. A. Schmidt, Investigation of high-temperature degradation of platinum thin films with an in situ resistance measurement apparatus. *J. Microelectromech. Syst.* **7**, 128–135 (1998).
  38. E. Çiftiyürek, K. Sabolsky, E. Sabolsky, Platinum thin film electrodes for high-temperature chemical sensor applications. *Sens. Actuators B* **181**, 702–714 (2013).
  39. S. Burger, C. Eberl, A. Siegel, A. Ludwig, O. Kraft, A novel high-throughput fatigue testing method for metallic thin films. *Sci. Technol. Adv. Mater.* **12**, 054202 (2011).
  40. J. Ausra, M. Wu, X. Zhang, A. Vázquez-Guardado, P. Skelton, R. Peralta, R. Avila, T. Murickan, C. R. Haney, Y. Huang, J. A. Rogers, Y. Kozorovitskiy, P. Gutruf, Wireless, battery-free, subdermally implantable platforms for transcranial and long-range optogenetics in freely moving animals. *Proc. Natl. Acad. Sci. U.S.A.* **118**, e2025775118 (2021).
  41. J. Ausra, S. J. Munger, A. Azami, A. Burton, R. Peralta, J. E. Miller, P. Gutruf, Wireless battery free fully implantable multimodal recording and neuromodulation tools for songbirds. *Nat. Commun.* **12**, 1968 (2021).
  42. A. Burton, S. N. Obaid, A. Vázquez-Guardado, M. B. Schmit, T. Stuart, L. Cai, Z. Chen, I. Kandel, C. R. Haney, E. A. Waters, H. Cai, J. A. Rogers, L. Lu, P. Gutruf, Wireless, battery-free subdermally implantable photometry systems for chronic recording of neural dynamics. *Proc. Natl. Acad. Sci. U.S.A.* **117**, 2835–2845 (2020).
  43. S. Gargiulo, A. Greco, M. Gramanzini, M. P. Petretta, A. Ferro, M. Larobina, M. Panico, A. Brunetti, A. Cuocolo, PET/CT imaging in mouse models of myocardial ischemia. *J. Biomed. Biotechnol.* **2012**, 541872 (2012).
  44. L. Cai, A. Burton, D. A. Gonzales, K. A. Kasper, A. Azami, R. Peralta, M. Johnson, J. A. Bakall, E. Barron Villalobos, E. C. Ross, J. A. Szivek, D. S. Margolis, P. Gutruf, Osseosurface electronics—Thin, wireless, battery-free and multimodal musculoskeletal biointerfaces. *Nat. Commun.* **12**, 6707 (2021).
  45. L. Qian, X. Song, H. Ren, J. Gong, S. Cheng, Mitochondrial mechanism of heat stress-induced injury in rat cardiomyocyte. *Cell Stress Chaperones* **9**, 281–293 (2004).
  46. H. M. Peixoto, R. M. S. Cruz, T. C. Moulin, R. N. Leão, Modeling the effect of temperature on membrane response of light stimulation in optogenetically-targeted neurons. *Front. Comput. Neurosci.* **14**, 5 (2020).
  47. S. R. Pasadyn, M. Soudan, M. Gillinov, P. Houghtaling, D. Phelan, N. Gillinov, B. Bittel, M. Y. Desai, Accuracy of commercially available heart rate monitors in athletes: A prospective study. *Cardiovasc. Diagn. Ther.* **9**, 379–385 (2019).
  48. P. Dilaveris, C. K. Antoniou, P. Manolakou, I. Skiadas, K. Konstantinou, N. Magkas, P. Xydis, C. Chrysohoou, K. Gatzoulis, D. Tousoulis, Comparison of left ventricular and biventricular pacing: Rationale and clinical implications. *Anatol. J. Cardiol.* **22**, 132–139 (2019).
  49. K. Kim, M. Vöröslakos, J. P. Seymour, K. D. Wise, G. Buzsáki, E. Yoon, Artifact-free and high-temporal-resolution in vivo opto-electrophysiology with microLED optoelectrodes. *Nat. Commun.* **11**, 2063 (2020).
  50. L. M. Swift, R. Jaimes III, D. McCullough, M. Burke, M. Reilly, T. Maeda, H. Zhang, N. Ishibashi, J. M. Rogers, N. G. Posnack, Optocardiography and electrophysiology studies of ex vivo langendorff-perfused hearts. *J. Vis. Exp.* 10.3791/60472 (2019).
  51. P. Jirkof, Effects of experimental housing conditions on recovery of laboratory mice. *Lab Anim. (NY)* **44**, 65–70 (2015).
  52. A. Burton, S. M. Won, A. K. Sohrabi, T. Stuart, A. Amirhossein, J. U. Kim, Y. Park, A. Gabros, J. A. Rogers, F. Vitale, A. G. Richardson, P. Gutruf, Wireless, battery-free, and fully implantable electrical neurostimulation in freely moving rodents. *Microsystems Nanoeng.* **7**, 62 (2021).
  53. R. T. Yin, S. W. Chen, T. George, K. B. Lee, A. Murillo-berlioz, Abstract 14093: Open thoracic surgical implantation of cardiac pacemakers in rodents. *Circulation* **144**, (2021).

**Acknowledgments:** We thank B. Baggett for micro-CT usage. **Funding:** We acknowledge funding support from the National Heart, Lung, and Blood Institute NIH 5T32HL007955-19 (to J.A.), R01-HL141470 (to I.R.E. and M.M.), and R21-HL152324 (to I.R.E. and M.M.), the Leducq Foundation grant RHYTHM (to I.R.E.), the American Heart Association Predoctoral Fellowship 19PRE34380781 (to R.T.Y.), and the NIH 3OT2OD023848 (to J.A.B.). **Author contributions:** J.A. and P.G. designed devices and ex vivo experiments. J.A. fabricated devices and evaluated data. J.A., M.M., R.T.Y., S.A., and J.A.Br. performed ex vivo experiments. J.A., M.M., R.T.Y., and J.A.B. performed animal experiments. J.A.B. recorded the video of the heart for mechanical analysis. R.P. performed thermal and mechanical simulations. D.C. and J.A.Ba. rendered images. J.A., P.G., M.M., R.T.Y., I.R.E., and J.H. wrote the manuscript. **Competing interests:** The authors declare that they have no competing interests. **Data and materials availability:** All data needed to evaluate the results in this paper are available in the paper and/or the Supplementary Materials.

Submitted 29 April 2022  
 Accepted 6 September 2022  
 Published 26 October 2022  
 10.1126/sciadv.abq7469

## Wireless, fully implantable cardiac stimulation and recording with on-device computation for closed-loop pacing and defibrillation

Jokubas AusraMicah MadridRose T. YinJessica HannaSuzanne ArnottJaclyn A. BrennanRoberto PeraltaDavid ClausenJakob A. BakallIgor R. EfimovPhilipp Gutruf

*Sci. Adv.*, 8 (43), eabq7469. • DOI: 10.1126/sciadv.abq7469

### View the article online

<https://www.science.org/doi/10.1126/sciadv.abq7469>

### Permissions

<https://www.science.org/help/reprints-and-permissions>

Use of this article is subject to the [Terms of service](#)